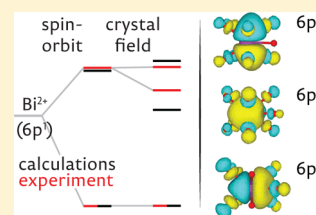


# Is Bi<sup>2+</sup> Responsible for the Red-Orange Emission of Bismuth-Doped SrB<sub>4</sub>O<sub>7</sub>?

Mathijs de Jong,<sup>†</sup> Andries Meijerink,<sup>†</sup> Robert A. Gordon,<sup>‡</sup> Zoila Barandiarán,<sup>§,||</sup> and Luis Seijo<sup>\*,§,||</sup><sup>†</sup>Condensed Matter and Interfaces, Debye Institute for Nanomaterials Science, Utrecht University, Princetonplein 5, 3584 CC Utrecht, The Netherlands<sup>‡</sup>Pacific Northwest Consortium Synchrotron Radiation Facility, APS Sector 20, Argonne, Illinois 60439, United States<sup>§</sup>Departamento de Química, Universidad Autónoma de Madrid, 28049 Madrid, Spain<sup>||</sup>Instituto Universitario de Ciencia de Materiales Nicolás Cabrera, Universidad Autónoma de Madrid, 28049 Madrid, Spain

## Supporting Information

**ABSTRACT:** Red-orange luminescence from bismuth-doped SrB<sub>4</sub>O<sub>7</sub> has previously been reported and assigned to 6p–6p transitions of divalent Bi. To provide support for this assignment and for the stability of this unusual valence state of Bi, we report here results from low-temperature luminescence spectroscopy, X-ray absorption near-edge structure (XANES) spectroscopy, electron paramagnetic resonance (EPR) spectroscopy, and wave function based ab initio calculations. Low-temperature luminescence spectra reveal zero-phonon lines (ZPLs) in excitation and emission spectra, allowing an accurate determination of the energies for the electronic transitions. The influence of the Bi concentration on the emission intensity is shown to be small, and only a small increase of the red-orange emission is observed upon raising the nominal Bi concentration from 0.02% (200 ppm) to 2%. This result indicates that only a very low concentration of Bi<sup>2+</sup> can be incorporated in SrB<sub>4</sub>O<sub>7</sub>. This observation is supported by EPR experiments, which do not show a signal that can be assigned to Bi<sup>2+</sup>, and by XANES experiments showing that most Bi is in the trivalent state. An upper limit of the Bi<sup>2+</sup> concentration is estimated to be 20 ppm. Ab initio calculations on the (BiO<sub>9</sub>)<sup>16–</sup> cluster embedded in SrB<sub>4</sub>O<sub>7</sub> give energies for excited states that are close to the experimentally observed energies. Also, the luminescence lifetime for the red-orange emission (~12 μs) is consistent with the lifetime for 6p–6p emission calculated for the Bi<sup>2+</sup> emission (3.5 μs). Equivalent ab initio calculations for Bi<sup>2+</sup> luminescence are very far from the experimental results, providing independent evidence and additional support for the interpretation of stable Bi<sup>2+</sup> species being responsible for the red-orange luminescence. The calculations provide a new interpretation of the third excitation band, which is not due to a <sup>2</sup>S<sub>1/2</sub> state of the 6s<sup>2</sup>7s configuration of Bi<sup>2+</sup>, as previously assumed, but is due to a state with important characters of 6s6p<sup>2</sup>–<sup>4</sup>P (63%) and doublets of the 6s6p<sup>2</sup>, 6s<sup>2</sup>6d, and 6s<sup>2</sup>6p configurations; its higher intensity is due to its character of parity-allowed 6s → 6p and 6p → 6d excitations.



## 1. INTRODUCTION

Divalent bismuth is rarely reported in inorganic chemistry textbooks. It was not until 1994 that the Bi<sup>2+</sup> species was considered to be stable by Blasse et al.<sup>1</sup> and to be responsible for the red-orange luminescence of bismuth-activated SrB<sub>4</sub>O<sub>7</sub>. By extension, Bi<sup>2+</sup> was assumed to cause the red luminescence of bismuth-activated alkaline earth sulfates already reported in 1886 by Lecoq de Boisbaudran<sup>2</sup> and of bismuth-activated phosphates reported in 1949 by Kröger et al.<sup>3</sup> (cf. ref 4). Recently, this ion has motivated a new approach in the search of new phosphors for energy-efficient solid-state lighting devices, and several reports on bismuth-activated luminescent materials have been published which assumed Bi<sup>2+</sup> as the active species.<sup>5–11</sup> This assumption was mainly supported on arguments that justify that the excitation and emission energies and the excited-state lifetime could not be explained by the participation of any other bismuth species but Bi<sup>2+</sup>.

In effect, the emission band and two excitation bands in the 17 000 and 21 000 cm<sup>–1</sup> regions in borates, sulfates, and phosphates have been interpreted to be due to local states

associated with the spin–orbit <sup>2</sup>P<sub>1/2</sub> and <sup>2</sup>P<sub>3/2</sub> levels of the 6s<sup>2</sup>6p configuration of Bi<sup>2+</sup>, the latter split under low-symmetry fields into <sup>2</sup>P<sub>3/2</sub>(1) and <sup>2</sup>P<sub>3/2</sub>(2) levels.<sup>1,5,8</sup> These are 6p → 6p parity-forbidden transitions in the free ion that become allowed in the host by the effect of the low-symmetry fields. A higher energy, more intense excitation band in the 40 000 cm<sup>–1</sup> region (also observed in bismuth-doped alkaline earth fluorides<sup>11</sup>) is attributed in all cases to a 6p → 7s transition: 6s<sup>2</sup>6p–<sup>2</sup>P<sub>1/2</sub> → 6s<sup>2</sup>7s–<sup>2</sup>S<sub>1/2</sub>. The fact that this is a parity-allowed transition in the free ion would explain its higher intensity.

While Bi can be found in compounds with formal valence ranging from –3 to +5, with even nonintegral valencies possible (e.g., in cluster compounds),<sup>12,13</sup> there is, however, little evidence for the existence of stable Bi<sup>2+</sup> active centers in solids apart from the optical spectroscopy measurements.

Received: March 26, 2014

Revised: April 15, 2014

Published: April 15, 2014

In this paper, we report results of several techniques aimed at clarifying the existence of a  $\text{Bi}^{2+}$  active center in bismuth-doped crystalline  $\text{SrB}_4\text{O}_7$  and at clarifying the assignment of the red-orange luminescence of this material.

We show experimental results of low-temperature excitation and emission spectra, X-ray absorption near-edge structure (XANES) measurements, and 20 K electron paramagnetic resonance (EPR) measurements. We also show *ab initio* calculations on the electronic structure of  $\text{Bi}^{2+}$  as a free ion and as a substitutional defect in  $\text{SrB}_4\text{O}_7$ . XANES and EPR do not give signals from  $\text{Bi}^{2+}$ . Luminescence experiments that supplement older measurements<sup>1</sup> detect the zero-phonon lines of  $^2\text{P}_{3/2}(1)$  and  $^2\text{P}_{3/2}(2)$  and indicate that the concentration of the red emitter is very low. *Ab initio* calculations provide details of energies, lifetimes, and nature of the  $\text{Bi}^{2+}$  electronic states as well as transition oscillator strengths. The overall agreement between the electronic structure of these states and the optical spectroscopic experiments provides strong support for the existence of  $\text{Bi}^{2+}$  and for the general interpretation of its luminescence. A new interpretation is provided for the third excitation to a higher state in the 40 000  $\text{cm}^{-1}$  region, which is found to be a configuration interaction mix of  $6s \rightarrow 6p$ ,  $6p \rightarrow 6d$ , and  $6p \rightarrow 7p$  excitations rather than a  $6p \rightarrow 7s$  transition.

The luminescence experiments are discussed in section 2, the XANES experiments in section 3, the EPR experiments in section 4, and the *ab initio* calculations in section 5. The conclusions are presented in section 6.

## 2. LUMINESCENCE

**A. Method.** Bismuth-doped  $\text{SrB}_4\text{O}_7$  was prepared as described by Blasse et al.<sup>1</sup> Stoichiometric amounts of  $\text{SrCO}_3$ ,  $\text{H}_3\text{BO}_3$ , and  $\text{Bi}_2\text{O}_3$  for 0.02%, 0.4%, and 2% bismuth concentrations were mixed and fired in  $\text{N}_2$  atmosphere first at 450 °C for 2 h and then at 840 °C for 8 h. Firing in reducing atmosphere ( $\text{H}_2$ ) yielded nonluminescent  $\text{SrB}_4\text{O}_7$ . Higher firing temperatures resulted in a glass material.

Luminescence spectra were recorded using an Edinburgh FLS920 spectrofluorometer with a 450 W xenon lamp as excitation source and a Hamamatsu R928 PMT as detector. For the low-temperature measurements, the spectrofluorometer was equipped with an Oxford Instruments helium cryostat. The decay times were measured using an Opotek Opolette 355 tunable laser in combination with the FLS920 spectrofluorometer, a Hamamatsu H7422-02 PMT, and an EG&G Ortec Turbo-MCS.

**B. Zero-Phonon Lines.** The 4.2 K excitation and emission spectra of bismuth-doped  $\text{SrB}_4\text{O}_7$  are shown in Figure 1. Sharp zero-phonon lines are visible in the emission spectrum and in the two first bands of the excitation spectrum. Although the excitation and emission spectra of this material have been measured before,<sup>1,7</sup> the energies of the zero-phonon lines have not been reported. Precise values of 17 245 and 20 705  $\text{cm}^{-1}$  (Table 1) are found for the  $^2\text{P}_{1/2} \rightarrow ^2\text{P}_{3/2}(1)$  and  $^2\text{P}_{1/2} \rightarrow ^2\text{P}_{3/2}(2)$  transitions, respectively.

The fine structure of the excitation band at high energy could not be resolved, and the energy level of this higher excited state was therefore chosen as the maximum of this excitation band. The integrated excitation intensity, which is a product of the absorption strength and the quantum efficiency for luminescence resulting from the excitation, was obtained by integrating the excitation bands in the spectrum. The values are listed in Table 1.

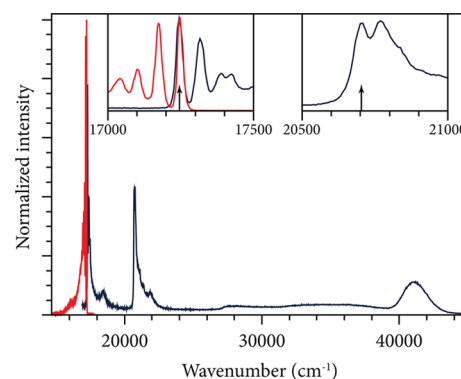


**Figure 1.** Low-temperature (4.2 K) excitation spectrum (blue line, emission at 620 nm) and emission spectrum (red line, excitation at 480 nm) of  $\text{SrB}_4\text{O}_7$  doped with 0.02% bismuth. Spectra are corrected for the intensity of the lamp in combination with the excitation monochromator and for the detector sensitivity in combination with the emission monochromator. The spectrum was converted from wavelength to energy scale, including the correction for the spectral distribution. The insets show in more detail the parts of the spectrum where the zero-phonon lines of the  $^2\text{P}_{1/2} \leftrightarrow ^2\text{P}_{3/2}(1)$  transitions (left inset) and  $^2\text{P}_{1/2} \rightarrow ^2\text{P}_{3/2}(2)$  transition (right inset) are located.

**Table 1. Experimental Energy Levels, in  $\text{cm}^{-1}$ , and Integrated Excitation Intensities Relative to  $^2\text{P}_{1/2} \rightarrow ^2\text{P}_{3/2}(1)$**

level <sup>a</sup>	main character <sup>a</sup>	energy	excitation intensity
$1\text{E}_{1/2}$	$^2\text{P}_{1/2}$	0	
$2\text{E}_{1/2}$	$^2\text{P}_{3/2}(1)$	17 245 (ZPL)	1.00
$3\text{E}_{1/2}$	$^2\text{P}_{3/2}(2)$	20 705 (ZPL)	0.98
$4\text{E}_{1/2}$	63% $^4\text{P}$	41 100 (max)	1.38

<sup>a</sup>This work assignment (cf. section 5).

**C. Concentration Dependence.** An analysis of the dependence of the emission intensity on the bismuth concentration reveals more about the incorporation of the bismuth in a divalent state in the  $\text{SrB}_4\text{O}_7$  lattice. For three concentrations of bismuth, an emission spectrum is shown in Figure 2. While there is a large variation in the bismuth concentrations in the starting material (from 0.02% to 2% there is a 100-fold increase), the emission intensity only varies slightly (from 0.02% to 2% there is a 2.3-fold increase).

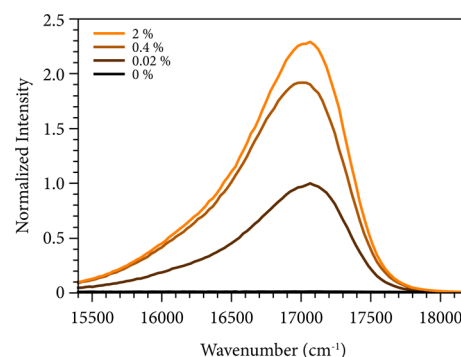


**Figure 2.** Emission spectra for a variety of bismuth-doping concentrations of  $\text{SrB}_4\text{O}_7$ . The spectra are normalized to the emission maximum of the 0.02% doped material. While there is a 100-fold increase in bismuth concentration in the starting mixture of the synthesis for the samples with 0.02% and 2% bismuth, there is only a 2.3-fold increase in emission intensity.

To investigate whether a quenching effect plays a role at higher bismuth concentrations, time-resolved emission measurements were done. The emission showed a monoexponential decay, shown in Figure 3. There is only a small decrease in the decay time at higher concentrations, which cannot explain the limited increase of emission intensity as a concentration quenching effect.

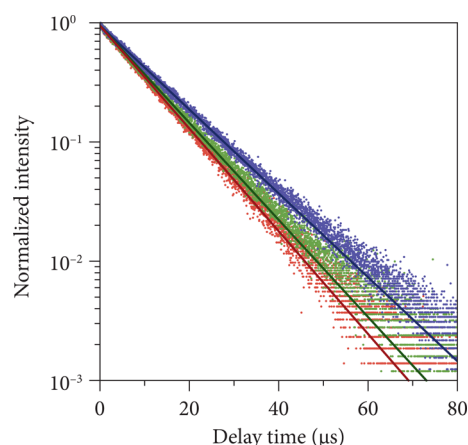


**Figure 3.** Emission decay curves of 0.02% (blue), 0.4% (green), and 2% (red) bismuth-doped  $\text{SrB}_4\text{O}_7$ . The decay times corresponding to the monoexponential fits are, respectively, 12.3, 10.7, and 10.1  $\mu\text{s}$ .

From the integrated emission intensities and the emission decay times, it can be concluded that upon increasing the bismuth concentration in the synthesis starting mixture, only a small fraction of this bismuth ends up in the  $\text{SrB}_4\text{O}_7$  lattice in a divalent state. This is in line with the knowledge that 2+ is not a stable oxidation state for bismuth, unlike 3+ and 5+. This suggests that also at 0.02% doping concentration only a part of the bismuth is incorporated as  $\text{Bi}^{2+}$  and that the concentration of the  $\text{Bi}^{2+}$  ion in our experiments is possibly much lower than 0.02% (200 ppm).

### 3. XANES EXPERIMENTS

**A. Method.** X-ray absorption near-edge structure (XANES) spectroscopic measurements at the Bi LIII edge were performed at beamline 20BM (PNC/XSD) at the Advanced Photon Source (APS). Incident X-rays from a Si(111) double-crystal monochromator were either toroidally focused to a spot size of 500 by 400  $\mu\text{m}^2$  (0.02% doping sample) or unfocused (2% and  $\text{Bi}_2\text{O}_3$  reference). For focused mode, a 0.3 mm high white beam slit 25 m from the bending magnet source was used versus 0.5 mm high for unfocused mode with sample slit height 0.9 mm at 50 m from the source. The X-ray monochromator was detuned to 80% of the maximum signal at 13.700 keV, and a Rh-coated planar mirror at 3.5 mrad angle was also used for harmonic rejection. Fluorescent X-rays were monitored using a 12-element germanium detector (Canberra) and transmission ion chambers ( $\text{N}_2$ -filled) for transmission. A 10  $\mu\text{m}$  thick Bi foil (Goodfellow) was used to monitor energy calibration after the sample-transmission ion chamber. Samples were measured as pellet (0.02% doped), packed powder (2%), or powder on kapton tape ( $\text{Bi}_2\text{O}_3$ , eight layers, measured in transmission).

**B. Bismuth Oxidation States in  $\text{SrB}_4\text{O}_7$ .** XANES spectra for 0.02% and 2% doped  $\text{SrB}_4\text{O}_7$  along with reference Bi metal foil and  $\text{Bi}_2\text{O}_3$  are overlaid in Figure 4. Background removal and normalization to unit edge step were done using the program

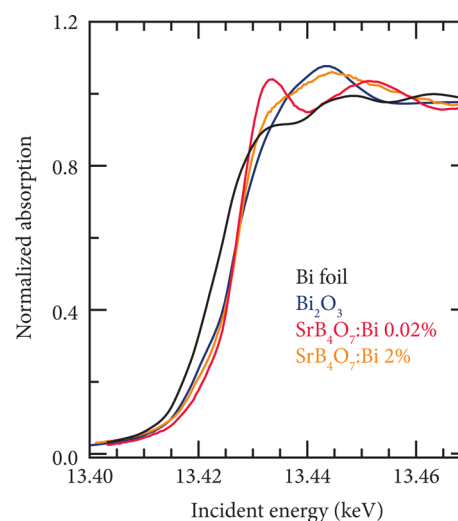


**Figure 4.** Comparison of normalized XANES spectra for 0.02% and 2% bismuth-doped  $\text{SrB}_4\text{O}_7$  with reference spectra for Bi foil and  $\text{Bi}_2\text{O}_3$ .

WinXAS.<sup>14</sup> Compared to the foil, the trivalent oxide reference exhibits a shift to higher binding energy in absorption, where the reduced 6p valence electron occupation reduces the screening of the core 2p and valence 6d states from the nuclear charge. A pronounced difference in structure is evident between the oxide and the 0.02%-doped data. Different local Bi environments can cause such changes.<sup>15</sup> The 2%-doped sample has features reminiscent of both the oxide and the 0.02%-doped samples, suggesting the sample is mixed phase and the doping level is only nominally 2% on the basis of the starting level and not of the end product.

Considering the 0.02% result in more detail, we note that the edge position for this sample is comparable to that for the trivalent oxide. This is strongly suggestive that the dominant contribution to the XANES is from a trivalent Bi species. If the dominant Bi species were divalent, one would expect the presence of a 6p valence electron to correlate with a smaller edge shift from the Bi metal foil position. For this reason, only a fraction of the 200 ppm bismuth could be in a divalent state below detection levels for this method. An upper limit of 20 ppm  $\text{Bi}^{2+}$  is estimated. For more than 10% of Bi in the divalent state, a shift of the edge should be observable. This is consistent with the effects of concentration of starting material on luminescence intensity.

The Bi dopant concentration dependence of the XANES spectrum allows us to make a comment on the incorporation of  $\text{Bi}^{3+}$  in the  $\text{SrB}_4\text{O}_7$  lattice. We note the reduction in amplitude in the region just above the absorption onset between 13.420 and 13.425 keV and interpret such as a reduction in covalent interactions between Bi and O in the borate versus the oxide. If, as the XANES indicates, the Bi is entering the  $\text{SrB}_4\text{O}_7$  structure as a predominantly trivalent species, with  $\text{B}^{3+}$  substantially smaller than  $\text{Bi}^{3+}$  and  $\text{Sr}^{2+}$  slightly larger,<sup>16</sup> occupation of a Sr site is more probable. Charge balance would dictate that for every two substitutions, either an additional Sr vacancy must also be created or another anion, interstitial oxygen, must also be present. Either of these mechanisms could lead to a destabilizing of the structure and could lead to the limit in incorporation of  $\text{Bi}^{3+}$  observed in the nominal 2% doped sample. In considering what the doping limit may be, we compared linear combinations of the 0.02% doped  $\text{SrB}_4\text{O}_7$  (assumed only to be from substitution) and  $\text{Bi}_2\text{O}_3$  XANES



spectra to the 2% doped  $\text{SrB}_4\text{O}_7$  XANES spectrum and found the best agreement between ratios 30:70 and 40:60 for 0.02% doped  $\text{SrB}_4\text{O}_7\text{:Bi}_2\text{O}_3$ . The XANES spectra therefore suggest that the limit of  $\text{Bi}^{3+}$  incorporation is at most 0.6–0.8%.

#### 4. EPR EXPERIMENTS

An unpaired electron in an atomic orbital gives an ion a magnetic moment, which gives rise to an energy difference between the two possible orientations of the magnetic moment in a magnetic field. Electron paramagnetic resonance (EPR) spectroscopy makes use of this splitting, and this technique can prove the presence of unpaired electrons. The  $6s^26p$  ground state of  $\text{Bi}^{2+}$  has a single electron in a  $6p$  orbital, and the energy gap between the two orientations of the spin of this electron in the magnetic field can be measured.

For  $\text{Bi}^{2+}$ , this experiment was first done by Murphy et al.<sup>17</sup> They used a bismuth-doped  $\text{CdWO}_4$  crystal and measured an X-band EPR spectrum at 27 K after the material was irradiated with X-rays at 77 K. No EPR signal was observed before irradiation. The observed signal consists of peaks at  $g = 1.543$ ,  $g = 1.380$ , and  $g = 1.623$  for the three different crystallographic axes, split up in 10 components, which is expected from the coupling of the unpaired electron to the  $I = 9/2$  nuclear spin of  $^{209}\text{Bi}$ . It was necessary to keep the crystal at low temperature between irradiation with X-rays and the EPR experiment. This indicates that the  $\text{Bi}^{2+}$  ion in  $\text{CdWO}_4$  is not stable at room temperature.

According to our optical spectroscopy measurements,  $\text{Bi}^{2+}$  in  $\text{SrB}_4\text{O}_7$  is stable at room temperature in low concentrations. EPR measurements on non-irradiation-induced  $\text{Bi}^{2+}$  have not been reported before; therefore, an attempt was made to measure the unpaired electron in  $\text{SrB}_4\text{O}_7\text{:Bi}^{2+}$  at room temperature.

Room temperature and 20 and 40 K measurements were performed using a Bruker EPR spectrometer in the X-band (9.4 GHz).  $\text{SrB}_4\text{O}_7$  powders with bismuth dopant concentrations of 0.02%, 0.4%, and 2% were used. At room temperature, none of them showed any signal in the region from 0 to 1.6 T. At 20 and 40 K, only low concentrations of iron impurities were observed in a scan from 0 to 0.6 T, but no signal belonging to bismuth was recorded, even though  $\text{Bi}^{2+}$  should in principle be observable in this region as proven by Murphy et al.<sup>17</sup> Because EPR is a very sensitive technique, it indicates that if bismuth is present in a divalent state, this must be below the level of sensitivity of the measurement, similar to the XANES experiments.

#### 5. AB INITIO CALCULATIONS

**A. Method.** We performed ab initio wave function theory embedded cluster quantum chemical calculations on the  $(\text{BiO}_9)^{16-}$  cluster embedded in the  $\text{SrB}_4\text{O}_7$  host with the MOLCAS suite of programs.<sup>18</sup> They include Bi–O bonding effects, static and dynamic electron correlation effects, and scalar and spin–orbit coupling relativistic effects within the cluster as well as Coulomb, exchange, and Pauli repulsion embedding effects from the host onto the cluster. Electron correlation effects between the cluster and the host are excluded from these calculations. Because Bi substitutes for Sr in  $\text{SrB}_4\text{O}_7$  and Sr occupies a  $C_s$  point symmetry site,<sup>19</sup> most of the calculations have been performed using this symmetry, except for structures with Bi off-plane, where  $C_1$  symmetry was used instead.

The embedded cluster calculations are two-step spin–orbit coupling SA-CASSCF/MS-CASPT2/RASSI-SO DKH calculations. In the first step, we used the many-electron scalar relativistic second-order Douglas–Kroll–Hess (DKH) Hamiltonian.<sup>20,21</sup> We performed state-average complete-active-space self-consistent-field<sup>22–24</sup> (SA-CASSCF) calculations with the active space that results from distributing 3 electrons in 13 active molecular orbitals with main character Bi 6s, 6p, 6d, 7s, and 7p:  $[6s, 6p, 6d, 7s, 7p]^3$ . In  $C_s$  symmetry, the active space is  $[9 \times a', 4 \times a'']^3$ . In the SA-CASSCF calculations, the following energy averages were minimized: The average of 17 states derived from the lowest doublets of free  $\text{Bi}^{2+}$  ( $6s^26p-^2P^o$ ,  $6s^27s-^2S$ ,  $6s^26d-^2D$ ,  $6s6p^2-^2P$ ,  $6s6p^2-^2D$ ) and the average of the 3 states derived from the term  $6s6p^2-^4P$  of  $\text{Bi}^{2+}$ . In  $C_s$  symmetry, this means the independent averages of the first 11  $^2A'$ , 6  $^2A''$ , 2  $^4A'$ , and 1  $^4A''$  states. The SA-CASSCF calculations provided occupied and empty molecular orbitals to feed subsequent multistate second-order perturbation theory calculations (MS-CASPT2),<sup>25–28</sup> where the dynamic correlation of 85 electrons (the 5d, 6s, 6p electrons of Bi and the 2s, 2p electrons of the nine O atoms) were taken into account. We used the standard IPEA value (0.25 au).<sup>29</sup>

In the second step, we included spin–orbit coupling effects by adding the atomic mean field integral (AMFI) approximation of the DKH spin–orbit coupling operator<sup>30</sup> to the scalar relativistic Hamiltonian. In this step, we used the spin-free state-shifting operator as a means to combine spin–orbit couplings calculated with statically correlated wave functions and spin–orbit free energies calculated with dynamic correlation,<sup>31</sup> and accordingly, we performed restricted-active-space state-interaction spin–orbit calculations (RASSI-SO)<sup>32,33</sup> with the transformed CASSCF wave functions (first-order wave functions of the MS-CASPT2 method) and the MS-CASPT2 energies. We allowed the mixing of the first 17 doublets and 3 quartets. In  $C_s$  symmetry, they are 1–11  $^2A'$ , 1–6  $^2A''$ , 1–2  $^4A'$ , and 1  $^4A''$ , and they give 23  $E_{1/2}$  Kramers doublets. We also performed some calculations on the corresponding embedded cluster of  $\text{Bi}^{3+}$ ,  $(\text{BiO}_9)^{15-}$ , for comparisons. For these, we used the active space that results from distributing two electrons in four active molecular orbitals with main character Bi 6s and 6p:  $[6s, 6p]^2$ , and we computed the singlets and triplets related with the atomic  $6s^2-^1S$ ,  $6s6p-^1P^o$ , and  $6s6p-^3P^o$  and the spin–orbit coupling between them.

All the calculations are all-electron with atomic natural orbital (ANO) relativistic basis sets for bismuth and oxygen<sup>34</sup> with respective contractions  $(25s22p16d12f4g)/[11s10p9d6f4g]$  and  $(14s9p4d)/[4s3p2d]$ .

The Hamiltonian of the  $(\text{BiO}_9)^{16-}$  cluster was supplemented with the ab initio model potential (AIMP) embedding potential<sup>35</sup> of  $\text{SrB}_4\text{O}_7$ , which has been obtained in this work. It is available from the authors<sup>36</sup> and is presented as Supporting Information. This embedding potential is made of (1) total-ion embedding AIMP representing  $\text{Sr}^{2+}$  and  $\text{B}^{3+}$  cations and  $\text{O}^{2-}$  anions, which are located at experimental sites of the  $\text{SrB}_4\text{O}_7$  lattice within a cube made of  $3 \times 3 \times 3$  unit cells and which are centered on  $\text{Sr}^{2+}$ , and (2) a set of 16 584 additional point charges situated at lattice sites, generated by the zero-multipole method of Gellé and Lepetit,<sup>37</sup> which closely reproduces the Ewald potential<sup>38</sup> within the cluster. The experimental crystal structure of  $\text{SrB}_4\text{O}_7$  (ref 19) is the following: Space group number 31,  $\text{Pmn}2_1$  orthorhombic; lattice constants  $a = 10.711$  Å,  $b = 4.427$  Å,  $c = 4.235$  Å; two (a) sites occupied by Sr ( $y_{\text{Sr}} = 0.289$ ,  $z_{\text{Sr}} = 0$ ) and  $\text{O}_1$  ( $y_{\text{O}_1} = 0.728$ ,  $z_{\text{O}_1} = 0.454$ ) and four (b)

Table 2. Experimental and Calculated Spectra of Bi<sup>2+</sup> Free Ion<sup>a</sup>

main configuration	term	J	experiment <sup>b</sup>	this work	
				even SA weights	1–4 SA weights
6s <sup>2</sup> 6p	<sup>2</sup> P <sup>o</sup>	1/2	0	0	0
		3/2	20 788	18 811 (–1977)	20 345 (–443)
6s6p <sup>2</sup>	<sup>4</sup> P	1/2	70 254	73 654 (+3400)	73 406 (+3152)
		3/2	83 038	83 416 (+378)	83 876 (+838)
		5/2	89 236	88 979 (–257)	88 722 (–514)
6s <sup>2</sup> 7s	<sup>2</sup> S	1/2	95 075	93 875 (–1200)	94 404 (–671)
6s <sup>2</sup> 6d	<sup>2</sup> D	3/2	96 154	95 082 (–1072)	94 397 (–1757)
		5/2	102 446	99 834 (–2612)	101 101 (–1345)
6s6p <sup>2</sup>	<sup>2</sup> P	1/2	108 052	108 222 (+170)	109 200 (+1148)
		3/2	130 966	127 230 (–3736)	127 651 (–3315)
6s6p <sup>2</sup>	<sup>2</sup> D	3/2	108 586	105 595 (–2991)	105 550 (–3036)
		5/2	116 414	112 370 (–4044)	111 333 (–5081)
6s <sup>2</sup> 7p	<sup>2</sup> P <sup>o</sup>	1/2	116 993	115 477 (–1516)	117 045 (+52)
		3/2	122 128	119 846 (–2282)	121 240 (–888)
6s6p <sup>2</sup>	<sup>2</sup> S	1/2	130 986	128 275 (–2711)	129 488 (–1498)
rms deviation				2379	2158
Bi <sup>3+</sup> 6s <sup>2</sup>	<sup>1</sup> S	0	206 180	203 463 (–2717)	204 748 (–1432)

<sup>a</sup>Results of two calculations with different choices of state-average weights are shown; see text for details. Energies in cm<sup>–1</sup>. Deviations from experiments are shown in parentheses. <sup>b</sup>Reference 40.

sites occupied by O<sub>2</sub> ( $x_{O_2} = 0.359$ ,  $y_{O_2} = 0.857$ ,  $z_{O_2} = 0.064$ ), O<sub>3</sub> ( $x_{O_3} = 0.221$ ,  $y_{O_3} = 0.631$ ,  $z_{O_3} = 0.335$ ), O<sub>4</sub> ( $x_{O_4} = 0.365$ ,  $y_{O_4} = 0.226$ ,  $z_{O_4} = 0.335$ ), B<sub>1</sub> ( $x_{B_1} = 0.379$ ,  $y_{B_1} = 0.174$ ,  $z_{B_1} = 0.976$ ), and B<sub>2</sub> ( $x_{B_2} = 0.246$ ,  $y_{B_2} = 0.671$ ,  $z_{B_2} = 0.936$ ). The embedding AIMP has been obtained in self-consistent embedded-ions (SCEI)<sup>39</sup> Hartree–Fock (HF) calculations.

**B. Electronic Structure of Bi<sup>2+</sup> Free Ion.** It is interesting to know the performance of the present ab initio method in the Bi<sup>2+</sup> free ion because its electronic states are a reference for the states of Bi<sup>2+</sup> in SrB<sub>4</sub>O<sub>7</sub> and other solids.

In free Bi<sup>2+</sup>, we performed the same type of SA-CASSCF/MS-CASPT2/RASSI-SO DKH calculations as in the (BiO<sub>9</sub>)<sup>16–</sup> cluster. We used the same basis set, active space, and dynamic correlation described in section 5 A. For methodological convenience, we used *C<sub>i</sub>* symmetry. We used even weights for the states of separated SA-CASSCF calculations in <sup>2</sup>L<sup>o</sup> odd terms 6s<sup>2</sup>6p–<sup>2</sup>P<sup>o</sup> and 6s<sup>2</sup>7p–<sup>2</sup>P<sup>o</sup>; <sup>2</sup>L even terms 6s<sup>2</sup>7s–<sup>2</sup>S, 6s<sup>2</sup>6d–<sup>2</sup>D, 6s6p<sup>2</sup>–<sup>2</sup>P, <sup>2</sup>D, and <sup>2</sup>S; and <sup>4</sup>L even term 6s6p<sup>2</sup>–<sup>4</sup>P. The states are multiconfigurational, and only the main configurational characters are indicated. The results are shown in Table 2 in the column labeled “even SA weights”. We can observe a rather good agreement with the experimental energies<sup>40</sup> in all states under consideration with a root-mean-square deviation of 2380 cm<sup>–1</sup> in transitions starting in 20 000 cm<sup>–1</sup> and going as high as 130 000 cm<sup>–1</sup> and with a 6s<sup>2</sup>6p–<sup>2</sup>P<sup>o</sup> spin–orbit splitting of 18 811 cm<sup>–1</sup>, which underestimates the experiment by 9.5%.

Such underestimation of the spin–orbit splitting is in line with a 15% underestimation of the splitting in Tl obtained in spin–orbit configuration interaction (SOCI) calculations,<sup>41</sup> and it is related to the fact that the 6p<sub>1/2</sub> and 6p<sub>3/2</sub> spinors are not optimized with a spin–orbit Hamiltonian. In our calculations, the differences in the radial functions of these spinors result only from the orbital excitations considered in the configuration interaction step with the spin–orbit coupling Hamiltonian, so that when this difference is as large as in 6p elements the CI may be insufficient. In these cases, *jj*-coupling based methods

perform especially better than *LS*-coupling based methods like the present one.<sup>41</sup> In Bi<sup>2+</sup>, the configuration interaction between 6s<sup>2</sup>6p–<sup>2</sup>P<sup>o</sup> and 6s<sup>2</sup>7p–<sup>2</sup>P<sup>o</sup> allows us to obtain different 6p<sub>1/2</sub> and 6p<sub>3/2</sub> spinors via mixing of the 6p orbital with the 7p orbital in the so-called double-shell effect.<sup>42,43</sup> Thus, we explored here to what extent the different 6p–7p mixings resulting from using different state-average weights of the 6s<sup>2</sup>6p–<sup>2</sup>P<sup>o</sup> and 6s<sup>2</sup>7p–<sup>2</sup>P<sup>o</sup> states in the SA-CASSCF calculation can affect the <sup>2</sup>P<sup>o</sup> spin–orbit splitting. In Table 2 (column “1–4 SA weights”), we show the results of using relative weights of 1 and 4, respectively, for the states of the 6s<sup>2</sup>6p and 6s<sup>2</sup>7p configurations of the <sup>2</sup>P<sup>o</sup> block. Although less relevant for the <sup>2</sup>P<sup>o</sup> spin–orbit splitting, we also used relative weights of 1 for 6s<sup>2</sup>7s–<sup>2</sup>S, 6s<sup>2</sup>6d–<sup>2</sup>D, 6s6p<sup>2</sup>–<sup>2</sup>P, <sup>2</sup>D, and <sup>2</sup>S and of 4 for two additional <sup>2</sup>P, two <sup>2</sup>D, and two <sup>2</sup>S terms of the 6s6p7p configuration. We can see that the different 6p–7p mixings in the 6p<sub>1/2</sub> and 6p<sub>3/2</sub> spinors that result in this case improve the <sup>2</sup>P<sup>o</sup> spin–orbit splitting, reducing its underestimation of experiment to 2.1%. (The 1–4 SA weights increase the energy of the 6s<sup>2</sup>7p–<sup>2</sup>P<sup>o</sup> *J* = 1/2 and *J* = 3/2 states relative to the ground state with respect to the 1–1 SA weights because of the stronger spin–orbit coupling between 6s<sup>2</sup>6p–<sup>2</sup>P<sup>o</sup> and 6s<sup>2</sup>7p–<sup>2</sup>P<sup>o</sup> they produce; at the spin–orbit coupling free MS-CASPT2 level, the energy difference between these two terms is the same in the 1–4 and 1–1 calculations within 0.4%.) However, we must bear in mind that using this technique as a means to improve the 6p related spinors of Bi<sup>2+</sup> in solids demands averages of the 6s<sup>2</sup>6p–<sup>2</sup>P<sup>o</sup> related states with 6s<sup>2</sup>7p–<sup>2</sup>P<sup>o</sup> related states, which are very high in energy. This becomes impractical when the inversion center is lost, as in SrB<sub>4</sub>O<sub>7</sub>:Bi<sup>2+</sup>, because a large number of 6s<sup>2</sup>6d, 6s<sup>2</sup>6s, and 6s6p<sup>2</sup> related states are inserted between the target states of the state average.

**C. Electronic Structure of Bi<sup>2+</sup> in SrB<sub>4</sub>O<sub>7</sub>.** In this section, we show the computed energy levels of the (BiO<sub>9</sub>)<sup>16–</sup> cluster embedded in SrB<sub>4</sub>O<sub>7</sub>. The results correspond to the (ground and excited states) cluster structures resulting after the off-center relaxation of the position of Bi<sup>2+</sup> within the rigid O<sub>9</sub> cage

created by the stiff oxygen network of the diborate, which was made in ref 44 at the spin–orbit coupling level of calculation.  $\text{Bi}^{2+}$  was found to stay on the symmetry plane and off-center from the Sr site both in the ground state and in the two first excited states. The ground-state cluster structure is shown in Figure 5. There is one oxygen atom in the  $\sigma_{yz}$  symmetry plane

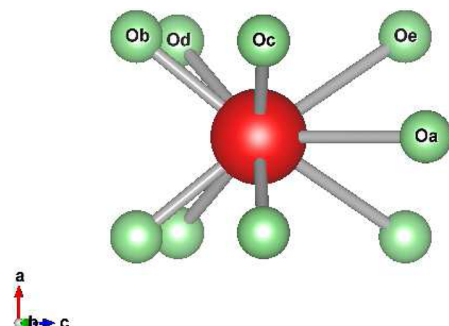


**Figure 5.**  $\text{BiO}_9$  moiety. The  $a$ ,  $b$ , and  $c$  axes of the  $\text{SrB}_4\text{O}_7$  orthorhombic lattice are shown.  $\text{O}_a$  is in the symmetry plane, which is perpendicular to the  $a$  axis;  $\text{O}_b$ ,  $\text{O}_c$ ,  $\text{O}_d$ , and  $\text{O}_e$  are out of plane, and their symmetry-related oxygens are unlabeled. The Bi–O distances in the unrelaxed host and in the ground-state relaxed host (in parentheses) are, in Å, Bi– $\text{O}_a$  2.73 (2.79), Bi– $\text{O}_b$  2.47 (2.39), Bi– $\text{O}_c$  2.68 (2.60), Bi– $\text{O}_d$  2.79 (2.81), and Bi– $\text{O}_e$  2.90 (3.02).

at 2.79 Å from Bi,  $\text{O}_a$ , and there are four sets of two off-plane symmetry related oxygen atoms: two at 2.39 Å,  $\text{O}_b$ ; two at 2.60 Å,  $\text{O}_c$ ; two at 2.81 Å,  $\text{O}_d$ ; and two at 3.02 Å,  $\text{O}_e$ .

**1. Spin–Orbit Coupling Free States.** Although the spin–orbit coupling splitting of the 6p shell of bismuth is so large that the electronic structure of  $\text{Bi}^{2+}$  in  $\text{SrB}_4\text{O}_7$  can only be understood at the spin–orbit coupling level, it is convenient to describe first the electronic states of the spin–orbit coupling free Hamiltonian and then later those of the full Hamiltonian in order to get insight. We summarize the spin–orbit free calculations in Table 3.

The  $6s^26p-^2P^0$  atomic term splits under the  $C_s$  effective field in three states spanning more than 12 000  $\text{cm}^{-1}$ . The interaction with higher atomic states is very small, and the

**Table 3. Lowest Energy Levels of the  $(\text{BiO}_9)^{16-}$  Cluster Embedded in  $\text{SrB}_4\text{O}_7$  Calculated without Spin–Orbit Coupling (MS-CASPT2 Level of Theory)<sup>a</sup>**

energy	level	configurational character
0	$1^2A''$	$a'(6s)^{1.98} a''(6p_x)^{0.99}$
4070	$1^2A'$	$a'(6s)^{1.98} a'(6p_y)^{0.99}$
12 450	$2^2A'$	$a'(6s)^{1.98} a'(6p_z)^{0.99}$
49 940	$1^4A''$	$a'(6s)^{1.00} a''(6p_x)^{1.00} a'(6p_y)^{1.00}$
53 760	$3^2A'$	$a'(6s)^{1.10} a''(6p_x)^{1.64} (2_a a')^{0.13} (3_a a')^{0.11b}$
53 810	$2^2A''$	dominant $6s6p^2$
54 490	$4^2A'$	dominant $6s6p^2$
58 320	$2^4A''$	$a'(6s)^{1.00} a''(6p_x)^{1.00} a'(6p_z)^{1.00}$
61 310	$5^2A'$	dominant $6s6p^2$
62 640	$1^4A'$	$a'(6s)^{1.00} a'(6p_y)^{1.00} a'(6p_z)^{1.00}$

<sup>a</sup>Point symmetry is  $C_s(yz)$ . Energies in  $\text{cm}^{-1}$ . Natural orbital main characters and occupations are shown. The NOs are represented in Figure 6; see ref 45 for an interactive representation. They are provided as Supporting Information. <sup>b</sup> $2_a a'$  and  $3_a a'$  are the second and third active  $a'$  NOs (with occupations lower than 2) of the  $3^2A'$  state; both of them are mainly mixtures of  $6p_y$ ,  $6p_z$ ,  $6d_{3x^2-r^2}$ , and  $6s$ .

three states have a highly dominant  $6s^26p$  configurational character, as it can be seen in the natural orbital (NO) populations. The shapes of the  $a'(6s)$ ,  $a''(6p_x)$ ,  $a'(6p_y)$ , and  $a'(6p_z)$  NOs are shown in the first row of Figure 6 (cf. ref 45

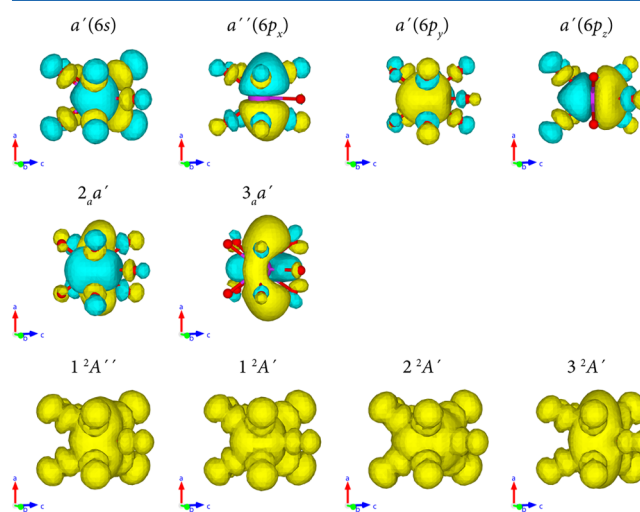


**Figure 6.** Active natural orbitals (rows 1 and 2) and electron densities (row 3) of the spin–orbit free states (MS-CASPT2 calculations). See Table 3. There are small differences between the NOs  $a'(6s)$ ,  $a''(6p_x)$ ,  $a'(6p_y)$ , and  $a'(6p_z)$  of different states, which are not visible in the scale of the figure.

for an interactive representation). The nodal planes between the oxygens and bismuth reveal the ionic character of their bonding interactions. The ground state is  $1^2A''$ , and it has the 6p electron in the  $a''(6p_x)$  antisymmetric orbital, which points perpendicular to the  $\sigma_{yz}$  symmetry plane in a direction between the four  $\text{O}_b$ ,  $\text{O}_c$ ,  $\text{O}_d$ , and  $\text{O}_e$  atoms each side of the plane, with lowest electrostatic repulsion with them. This orbital has a nonbonding character with the in-plane  $\text{O}_a$  atom. The first excited state is  $1^2A'$ , and it has the 6p electron in the  $a'(6p_y)$  symmetric orbital with two nonequivalent lobes, the biggest one pointing toward the empty space between four oxygens (two  $\text{O}_d$  and two  $\text{O}_e$ ) and the smallest one pointing toward the midpoint between the two  $\text{O}_c$  atoms. Because this orientation is more repulsive than that of  $a''(6p_x)$ ,  $1^2A'$  is above  $1^2A''$  in energy. The  $a'(6p_y)$  NO has an almost nonbonding character with the two  $\text{O}_b$  atoms, which lie very close to its nodal plane. The second excited state is  $2^2A'$ , and it has the 6p electron in the  $a'(6p_z)$  symmetric orbital also with two nonequivalent lobes, the biggest one pointing toward the in-plane  $\text{O}_a$  atom and the smallest one pointing toward the midpoint between the two  $\text{O}_b$  atoms. This orientation is significantly more repulsive than the previous ones and, as a consequence, the  $2^2A'$  state lies at a significantly larger energy. The  $a'(6p_z)$  NO has nonbonding character with the two  $\text{O}_c$  atoms, which lie in its nodal plane.

The lowest state of the  $C_s$  splitting of the  $6s6p^2-^4P$  atomic term is the third excited state,  $1^4A''$ . It has an almost pure  $a'(6s)a''(6p_x)a'(6p_y)$  configurational character with the two 6p electrons occupying the two most stable  $C_s$ -split 6p orbitals. The  $6s \rightarrow 6p$  excitation implicit in this state makes it appear more than 35 000  $\text{cm}^{-1}$  above the highest  $^2P^0$  related state.

A group of states starts at about 4000  $\text{cm}^{-1}$  above the latter, the lowest one lying 53 760  $\text{cm}^{-1}$  above the  $1^2A''$  ground state and having a strong mixture of  $6s6p^2$ ,  $6s^26d$ , and  $6s^27p$



**Table 4.** Lowest  $E_{1/2}$  Kramers Doublets of  $(\text{BiO}_9)^{16-}$  Embedded in  $\text{SrB}_4\text{O}_7$  ( $C_s'$  Double Group) Computed at the Ground-State Structure Using the Spin–Orbit Coupling Hamiltonian (RASSI-SO Level of Theory). Energies Relative to the Ground State ( $\text{cm}^{-1}$ ), Absorption Oscillator Strengths, and Analysis of the Wave Functions in Terms of Their Spin–Orbit Free Characters (Contributions Larger than 5% Are Given)

state	energy	$f_{\text{abs}}$	percentage contributions of spin–orbit free states			
$1E_{1/2}$	0		53.9 1 $^2A''$	31.4 1 $^2A'$	14.5 2 $^2A'$	
$2E_{1/2}$	14 450	$4.2 \times 10^{-4}$	55.7 1 $^2A'$	42.0 1 $^2A''$		
$3E_{1/2}$	21 830	$1.1 \times 10^{-3}$	83.0 2 $^2A'$	12.8 1 $^2A'$		
$4E_{1/2}$	47 260	$1.3 \times 10^{-1}$	39.5 1 $^4A''$	15.2 2 $^4A''$	10.7 3 $^2A'$	8.4 1 $^4A'$
				8.4 5 $^2A'$	7.8 2 $^2A''$	
$5E_{1/2}$	56 070	$3.7 \times 10^{-3}$	85.1 1 $^4A''$	6.2 2 $^4A''$		
$6E_{1/2}$	59 520	$2.6 \times 10^{-1}$	54.4 2 $^2A''$	23.2 1 $^4A''$	9.5 2 $^4A''$	5.0 5 $^2A''$

configurations. Its natural orbital occupations are  $a'(6s)^{1.10}$   $a''(6p_x)^{1.64}$   $(2a'a')^{0.13}$   $(3a'a')^{0.11}$ ; the populations of  $a'(6s)$  and  $a''(6p_x)$  indicate the strong configurational mixing, and the second and third active  $a'$  NOs,  $2a'a'$  and  $3a'a'$ , which allocate together 0.25 electrons, are mainly mixtures of  $6p_y$ ,  $6p_z$ ,  $6d_{3x^2-r^2}$ , and  $6s$ . They are shown in the second row in Figure 6. We did not see significant contributions from the  $6s^27s$  configuration up to  $70\,000\text{ cm}^{-1}$ ; let us remember that  $6s^27s-^2S_{1/2}$  has been assumed to be the third excited state.<sup>1,5,7</sup>

**2. States Including Spin–Orbit Coupling.** All the states of the full Hamiltonian are Kramers doublets that belong to the  $E_{1/2}$  irreducible representation of the  $C_s'$  double group. The relative energies and spin–orbit free characters of the lowest states computed with the ground-state equilibrium structure are shown in Table 4 together with the absorption oscillator strengths.

The spin–orbit coupling interactions between the three lowest spin–orbit free states, all of them of  $6s^26p-^2P^o$  character, dominate the three lowest  $E_{1/2}$  states. The contributions from higher spin–orbit free states are indeed very small. In Figure 7, we present a quantitative diagram of the

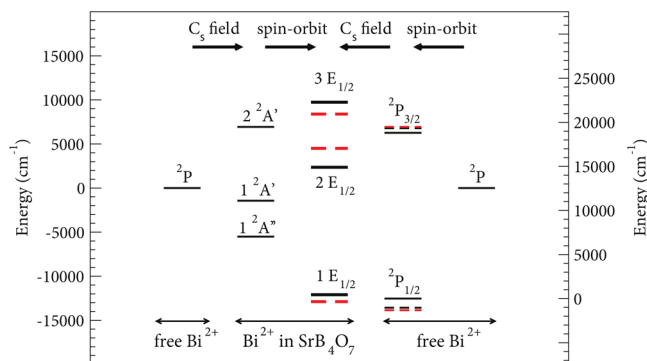


**Figure 7.** Quantitative correlation level diagram. Black lines: ab initio calculations; free-ion results using 1–4 state-average weights (last column in Table 2) are shown in dashed lines. Red dashed lines: experiments. See text for details.

1–3  $E_{1/2}$  energy levels together with the spin–orbit free counterparts  $1^2A''$ ,  $1^2A'$ , and  $2^2A'$  and the computed free-ion levels  $^2P_{1/2}$  and  $^2P_{3/2}$ . We show all of them in a common energy scale in which their respective averages and the  $\text{Bi}^{2+}$  free-ion spin–orbit coupling free term  $^2P$  are set to zero (left scale). In this scale, the difference between  $1E_{1/2}$  and  $^2P_{1/2}$  is  $450\text{ cm}^{-1}$ , and the difference between the average energy of  $2E_{1/2}$  and  $3E_{1/2}$  and  $^2P_{3/2}$  is  $-220\text{ cm}^{-1}$ . This shows the very small influence of excited configurations on the  $6s^26p-^2P$  related

states. In black dashed lines, we show the theoretical results of using state-average weights 1 and 4 for the  $6s^26p-^2P$  and  $6s^27p-^2P$  states in the SA-CASSCF step of the calculations of  $\text{Bi}^{2+}$  free ion. This result agrees very well with the experiment shown in red dashed lines. Such an agreement is because this state-averaging corrects the deficiencies of the spin–orbit coupling, compare section 5 B. However, we cannot use these state-average weights in our  $(\text{BiO}_9)^{16-}$  embedded cluster calculation because the states related with the  $6s^27p$  configuration are very high in energy. Thus, according to this result, we must expect our calculation to underestimate the average energy of the two first excited states with respect to the ground state.

The third excited state  $4E_{1/2}$ , which is assumed to have a  $6s^27s-^2S_{1/2}$  main character in the literature,<sup>1,5,7–11</sup> has a 63% character of  $6s6p^2-^4P$ . The rest of its character is spread over several doublets of  $6s6p^2$ ,  $6s^26d$ , and  $6s^27p$  configurations with no sign of relevant  $6s^27s$  character. The larger value of the absorption oscillator strength from the ground state to  $4E_{1/2}$  with respect to the previous two excited states must be associated, then, to the partial  $6s \rightarrow 6p$  and  $6p \rightarrow 6d$  characters involved in the  $1E_{1/2} \rightarrow 4E_{1/2}$  absorption.

The computed radiative lifetime of the  $2E_{1/2}$  state, which is responsible for the red-orange emission, is  $\tau_{0,\text{rad}} = 17\text{ }\mu\text{s}$  in vacuo. After including standard local field corrections<sup>46</sup> calculated with a refraction index of  $\text{SrB}_4\text{O}_7$   $n = 1.74$  (ref 47), the lifetime in the solid is  $3.5\text{ }\mu\text{s}$ . This means a local field reduction by a factor of 4.9. Lifetimes of other excited states computed with the same correction are shown in Figure 8.

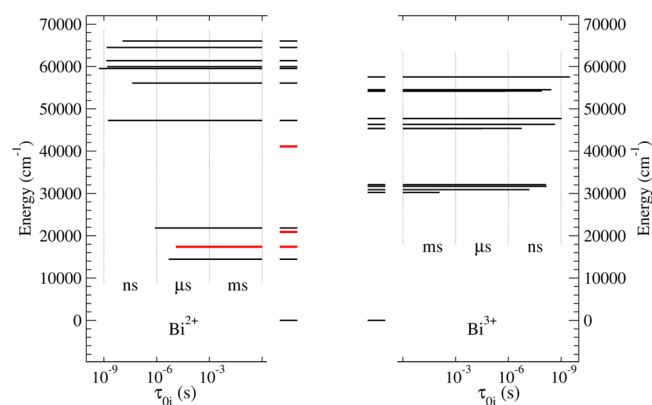


**Figure 8.** Energy levels and radiative lifetimes of the states of  $\text{Bi}^{2+}$  and  $\text{Bi}^{3+}$  in  $\text{SrB}_4\text{O}_7$ . Black: ab initio calculations. Red: experimental results attributed to the  $\text{Bi}^{2+}$  defect.

Table 5. Excitation Maxima (max ↑), Emission Maxima (max ↓), Zero-Phonon Lines (ZPL), Spin–Orbit Coupling Splittings,  $C_s$  Field Splittings, Absorption Oscillator Strengths ( $f_{\text{abs}}$ ), and Radiative Lifetimes<sup>a</sup>

		experiment	ab initio	
		energy	energy	$f_{\text{abs}}$
$1E_{1/2}[^2P_{1/2}^o(2)]$		0	0	
$2E_{1/2}[^2P_{3/2}^o(1)]$	max ↑	17 390 <sup>b</sup>	14 450	$4.2 \times 10^{-4}$
		17 300 <sup>c</sup>		
	max ↓	17 065 <sup>b</sup>	14 330	
		17 000 <sup>c</sup>		
	ZPL	17 245 <sup>d</sup>	14 370	
$3E_{1/2}[^2P_{3/2}^o(2)]$	max ↑	21 275 <sup>b</sup>	21 830	$1.1 \times 10^{-3}$
		20 900 <sup>c</sup>		
	ZPL	20 705 <sup>d</sup>	21 590	
$^2S_{1/2}(6s^27s)^e$	max ↑	>32 000 <sup>b</sup>		
		40 800 <sup>c</sup>		
$4E_{1/2}(6s6p^2, 6s^26d, 6s^27p)^f$		41 100 <sup>d</sup>	47 260	$1.3 \times 10^{-1}$
$^2P^o$ SO splitting		18 975 <sup>d</sup>	17 980	
$^2P_{3/2}^o$ $C_s$ splitting		3460 <sup>d</sup>	7220	
$2E_{1/2}[^2P_{3/2}^o(1)]$ lifetime ( $\mu\text{s}$ )		10.2 <sup>b</sup>	3.5	
		13.0 <sup>c</sup>		
		12.6 <sup>d</sup>		

<sup>a</sup>Energies in  $\text{cm}^{-1}$ . <sup>b</sup>Reference 1. <sup>c</sup>Reference 7. <sup>d</sup>This work. <sup>e</sup>Assignment of the third excitation band in refs 1 and 7. <sup>f</sup>Assignment of the third excitation band in this work.

**D. Comparisons with Experiments.** The comparisons between the ab initio calculations and the experimental data are summarized in Table 5 and Figure 8.

The pattern of excited states agrees with the experimental excitation spectra: two states in the  $20\,000\text{ cm}^{-1}$  region of comparable excitation intensities and no other state up to the  $40\,000\text{ cm}^{-1}$  region, where there is a third excitation of higher intensity. The data in Table 5 show a  $2875\text{ cm}^{-1}$  underestimation of the first excited state  $2E_{1/2}[^2P_{3/2}^o(1)]$  and  $885\text{ cm}^{-1}$  overestimation of the second,  $3E_{1/2}[^2P_{3/2}^o(2)]$ . We can take the average of these two states as the spin–orbit splitting of  $\text{Bi}^{2+}$   $^2P$  in the host and their difference as a measure of the  $C_s$  field splitting. Then, we get a theoretical spin–orbit splitting of  $17\,980\text{ cm}^{-1}$ , which is 95% of the experimental  $18\,975\text{ cm}^{-1}$ . The origin of this underestimation is the same as in free  $\text{Bi}^{2+}$ , where the theoretical spin–orbit splitting of the  $^2P^o$  term at the same level of calculation was 91% of the experimental value (cf. Table 2). As discussed in section 5 B, the reason is that the two-step spin–orbit method used here uses a few degrees of freedom to produce different radial functions for the  $6p_{1/2}$  and  $6p_{3/2}$  spinors and, hence, the underestimation. Whereas correcting this via state-average weights was possible in free  $\text{Bi}^{2+}$ , it is not in the  $(\text{BiO}_9)^{16-}$  embedded cluster because the necessary spin–orbit free states to be mixed are very high in energy. Concerning the  $C_s$  field splitting, the calculations overestimate that of  $^2P_{3/2}$ :  $7220\text{ cm}^{-1}$  versus  $3460\text{ cm}^{-1}$ . This overestimation is consistent with the lack of lattice relaxation effects in the calculations because oxygen displacements away from the  $\text{Bi}^{2+}$  impurity would lower the splitting. It cannot be ruled out that it is due in part to an overestimation of repulsive effects in the  $\text{SrB}_4\text{O}_7$  embedding potential.

The computed absorption oscillator strengths of the second and third bands are 2.6 and 310 times larger than that of the first band. These values are different from the experimentally observed ratios of 0.98 and 1.38. Especially, the high-energy band around  $41\,000\text{ cm}^{-1}$  is weaker than expected in the excitation spectrum. The low intensity can be due to direct nonradiative decay from this high-energy state to the ground

state (not yielding emission) or, more likely, to competing absorption from defects or  $\text{Bi}^{3+}$  also not giving rise to the orange emission that is monitored in the excitation spectrum.

The  $3.5\text{ }\mu\text{s}$  for the computed radiative lifetime of the emitting state  $2E_{1/2}[^2P_{3/2}^o(1)]$  is not far from the experimental values, which range between 10 and  $13\text{ }\mu\text{s}$ . In Figure 8, we present a graphic comparison with the experiment and with radiative lifetimes of other states of  $\text{Bi}^{2+}$  and  $\text{Bi}^{3+}$  in  $\text{SrB}_4\text{O}_7$ . The energy levels and lifetimes of  $\text{Bi}^{3+}$  have been computed in calculations equivalent to the ones for  $\text{Bi}^{2+}$  using the  $(\text{BiO}_9)^{15-}$  embedded cluster. The only states with a lifetime in the range of the experimental measurements are the  $2E_{1/2}[^2P_{3/2}^o(1)]$  and  $3E_{1/2}[^2P_{3/2}^o(2)]$  states of  $\text{Bi}^{2+}$ , the only possible emitting state being the first of them. The lowest set of states of  $\text{Bi}^{3+}$  has one state with a lifetime in the millisecond regime (corresponding to a  $^3P_0 \rightarrow ^1S_0$  emission), and the others are in the nanosecond regime (corresponding to  $^3P_1 + ^1P_1 \rightarrow ^1S_0$  emissions), as it is usually found in the luminescence of  $\text{Bi}^{3+}$  in solid hosts.<sup>48,49</sup> This, together with its higher energy, rules out the consideration of a state in this set as a possible emitter.

The overall agreement between the ab initio calculations and the experimental optical measurements strongly supports the initial hypothesis of Blasse et al.<sup>1</sup> of stable  $\text{Bi}^{2+}$  species being responsible for the red-orange luminescence of bismuth-doped  $\text{SrB}_4\text{O}_7$ .

## 6. CONCLUSIONS

Low-temperature luminescence experiments give the zero-phonon lines of the blue excitation and the red-orange emission of bismuth-doped  $\text{SrB}_4\text{O}_7$ , which have been attributed to transitions between the  $^2P_{1/2}$  ground state and the  $^2P_{3/2}(1)$  and  $^2P_{3/2}(2)$  excited states of  $\text{Bi}^{2+}$  in a low-symmetry  $C_s$  site.<sup>1</sup> The influence of the Bi concentration on the emission intensity is small, and only a small increase of the red-orange emission is observed upon raising the nominal Bi concentration from 0.02% (200 ppm) to 2%. This result indicates that only a very low concentration of  $\text{Bi}^{2+}$  can be incorporated in  $\text{SrB}_4\text{O}_7$ . Its



upper limit is estimated to be 20 ppm. EPR measurements do not detect the presence of  $\text{Bi}^{2+}$ , and XANES results suggest  $\text{Bi}^{3+}$  as the dominant species, both indicating that stable divalent bismuth could only be present in very low concentration, below detection limits for these techniques. Wave function based ab initio calculations on the  $(\text{BiO}_9)^{16-}$  cluster embedded in  $\text{SrB}_4\text{O}_7$  provide independent, additional support to the interpretation of stable  $\text{Bi}^{2+}$  species being responsible for the red-orange luminescence of the material. The support is based on the agreement between calculated and experimental level energies and emitting state lifetime. Equivalent calculations for the  $\text{Bi}^{3+}$  species are very far from experiment.

The calculations provide a new interpretation of the third excitation band, which is not due to a  $^2\text{S}_{1/2}$  state of the  $6s^27s$  configuration of  $\text{Bi}^{2+}$ , as previously assumed, but to a state with important characters of  $6s6p^2-^4\text{P}$  (63%) and doublets of the  $6s6p^2$ ,  $6s^26d$ , and  $6s^26p$  configurations; its higher intensity is due to its character of parity-allowed  $6s \rightarrow 6p$  and  $6p \rightarrow 6d$  excitations.

In summary, although EPR and XANES do not give a direct proof of the presence of  $\text{Bi}^{2+}$ , luminescence and ab initio results coincide on attributing the red-orange luminescence of bismuth-doped  $\text{SrB}_4\text{O}_7$  to a stable  $\text{Bi}^{2+}$  species. The concentration of this species has a very low upper limit in the parts per million range.

## ■ ASSOCIATED CONTENT

### ■ Supporting Information

AIMP embedding potential of  $\text{SrB}_4\text{O}_7$ : total-ion embedding  $\text{Sr}^{2+}$ ,  $\text{B}^{3+}$ , and  $\text{O}^{2-}$  AIMPs and additional point charges in MOLCAS format.  $a'(6s)$ ,  $a''(6p_x)$ ,  $a'(6p_y)$ ,  $a'(6p_z)$ ,  $(2a')$ ,  $(3a')$  natural orbitals and  $1^2\text{A}'$  and  $1-3^2\text{A}'$  electron densities in cube format. This material is available free of charge via the Internet at <http://pubs.acs.org>

## ■ AUTHOR INFORMATION

### Corresponding Author

\*E-mail: [luis.seijo@uam.es](mailto:luis.seijo@uam.es).

### Notes

The authors declare no competing financial interest.

## ■ ACKNOWLEDGMENTS

This work was partly supported by a grant from Ministerio de Economía y Competitividad, Spain (Dirección General de Investigación y Gestión del Plan Nacional de I+D+I, MAT2011-24586), and was partly supported by the EU Marie Curie Initial Training Network LUMINET (316906). The PNC/XSD facilities at the APS are supported by the U.S. Department of Energy - Basic Energy Sciences, the Canadian Light Source, the University of Washington, and the Advanced Photon Source. Use of the APS was supported by the U.S. Department of Energy under Contract No. DE-AC02-06CH11357. We are grateful for the EPR experiments performed by Gabriele Panarelli in the lab of Edgar Groenen at Leiden University and for the EPR experiments performed in the lab of Karl Krämer at the University of Bern.

## ■ REFERENCES

- Blasse, G.; Meijerink, A.; Nomes, M.; Zuidema, J. Unusual Bismuth Luminescence in Strontium Tetraborate ( $\text{SrB}_4\text{O}_7\text{:Bi}$ ). *J. Phys. Chem. Solids* **1994**, *55*, 171–174.
- Lecoq de Boisbaudran, M. Fluorescence des Composés du Bismuth, Soumis à l'Effluve Électrique dans le Vide. *C. R. Acad. Sci. Paris* **1886**, *103*, 629–631.
- Kröger, F. A.; Overbeek, J. T. G.; Goorissen, J.; van den Boomgaard, J. Bismuth as Activator in Fluorescent Solids. *Trans Electrochem. Soc.* **1949**, *96*, 132–141.
- Hamstra, M. A.; Folkerts, H. F.; Blasse, G. Materials Chemistry Communications. Red Bismuth Emission in Alkaline-Earth-Metal Sulfates. *J. Mater. Chem.* **1994**, *4*, 1349–1350.
- Srivastava, A. M. Luminescence of Divalent Bismuth in  $\text{M}^{2+}\text{BPO}_5$  ( $\text{M}^{2+} = \text{Ba}^{2+}$ ,  $\text{Sr}^{2+}$  and  $\text{Ca}^{2+}$ ). *J. Lumin.* **1998**, *78*, 239–243.
- Zeng, Q.; Zhang, T.; Pei, Z.; Su, Q. Luminescence of Unusual Bismuth in Barium Borates ( $\text{BaB}_8\text{O}_{13}\text{:Bi}$ ). *J. Mater. Sci. Technol.* **1999**, *15*, 281–282.
- Peng, M.; Wondraczek, L.  $\text{Bi}^{2+}$ -Doped Strontium Borates for White-Light-Emitting Diodes. *Opt. Lett.* **2009**, *34*, 2885–2887.
- Peng, M.; Wondraczek, L. Photoluminescence of  $\text{Sr}_2\text{P}_2\text{O}_7\text{:Bi}^{2+}$  as a Red Phosphor for Additive Light Generation. *Opt. Lett.* **2010**, *35*, 2544–2546.
- Bai, Z.; Fujii, M.; Hasegawa, T.; Kitano, S.; Imakita, K.; Mizuhata, M.; Hayashi, S. Co-existence of Bi with Multiple Valence States in Zeolites. Controlling the Optical Properties by Annealing Atmosphere. *Opt. Mater.* **2012**, *34*, 821–825.
- Peng, M.; Lei, J.; Li, L.; Wondraczek, L.; Zhang, Q.; Qiu, J. Site-Specific Reduction of  $\text{Bi}^{4+}$  to  $\text{Bi}^{2+}$  in Bismuth-Doped Over-Stoichiometric Barium Phosphates. *J. Mater. Chem. C* **2013**, *1*, 5303–5308.
- Cao, R.; Zhang, F.; Liao, C.; Qiu, J. Yellow-to-Orange Emission from  $\text{Bi}^{2+}$ -Doped  $\text{RF}_2(\text{R}=\text{Ca}$  and  $\text{Sr})$  Phosphors. *Opt. Express* **2013**, *21*, 15728–15733.
- Barnes, A. C.; Guo, C.; Howells, W. S. Fast-Ion Conduction and the Structure of  $\beta\text{-Mg}_3\text{Bi}_2$ . *J. Phys.: Condens. Matter* **1994**, *6*, L467–L471.
- Ahmed, E.; Köhler, D.; Ruck, M. Room-Temperature Synthesis of Bismuth Clusters in Ionic Liquids and Crystal Growth of  $\text{Bi}_5(\text{AlCl}_4)_3$ . *Z. Anorg. Allg. Chem.* **2009**, *635*, 297–300.
- Ressler, T. WinXAS: a Program for X-ray Absorption Spectroscopy Data Analysis under MS-Windows. *J. Synchrotron Radiat.* **1998**, *5*, 118–122.
- McKeown, D. A.; Gan, H.; Pegg, I. L. X-ray Absorption Studies of Bismuth Valence and Local Environments in Borosilicate Waste Glasses. *J. Nucl. Mater.* **2012**, *420*, 116–122.
- Shannon, R. D. Revised Effective Ionic Radii and Systematic Studies of Interatomic Distances in Halides and Chalcogenides. *Acta Crystallogr. A* **1976**, *32*, 751–767.
- Murphy, H. J.; Stevens, K. T.; Garces, N. Y.; Moldovan, M.; Giles, N. C.; Halliburton, L. E. Optical and EPR Characterization of Point Defects in Bismuth-Doped  $\text{CdWO}_4$  Crystals. *Radiat. Eff. Defects Solids* **1999**, *149*, 273–278.
- Karlström, G.; Lindh, R.; Malmqvist, P. A.; Roos, B. O.; Ryde, U.; Veryazov, V.; Widmark, P. O.; Cossi, M.; Schimmelpennig, B.; Neogrady, P.; et al. MOLCAS: A Program Package for Computational Chemistry. *Comput. Mater. Sci.* **2003**, *28*, 222–239.
- Krogh-Moe, J. The Crystal Structure of Strontium Diborate  $\text{SrO}_2\text{B}_2\text{O}_3$ . *Acta Chem. Scand.* **1964**, *18*, 2055–2060.
- Douglas, M.; Kroll, N. M. Quantum Electrodynamical Corrections to the Fine Structure of Helium. *Ann. Phys. (N.Y.)* **1974**, *82*, 89–155.
- Hess, B. A. Relativistic Electronic-Structure Calculations Employing a Two-Component No-Pair Formalism with External-Field Projection Operators. *Phys. Rev. A* **1986**, *33*, 3742–3748.
- Roos, B. O.; Taylor, P. R.; Siegbahn, P. E. M. A Complete Active Space SCF Method (CASSCF) Using a Density-Matrix Formulated Super-CI Approach. *Chem. Phys.* **1980**, *48*, 157–173.
- Siegbahn, P. E. M.; Heiberg, A.; Roos, B. O.; Levy, B. Comparison of the Super-CI and the Newton-Raphson Scheme in the Complete Active Space SCF Method. *Phys. Scr.* **1980**, *21*, 323–327.
- Siegbahn, P. E. M.; Heiberg, A.; Almlöf, J.; Roos, B. O. The Complete Active Space SCF (CASSCF) Method in a Newton-

Raphson Formulation with Application to the HNO Molecule. *J. Chem. Phys.* **1981**, *74*, 2384–2396.

(25) Andersson, K.; Malmqvist, P.-A.; Roos, B. O.; Sadlej, A. J.; Wolinski, K. Second-Order Perturbation Theory with a CAS-SCF Reference Function. *J. Phys. Chem.* **1990**, *94*, 5483–5488.

(26) Andersson, K.; Malmqvist, P.-A.; Roos, B. O. Second-Order Perturbation Theory with a Complete Active Space Self-Consistent Field Reference Function. *J. Chem. Phys.* **1992**, *96*, 1218–1226.

(27) Zaitsevskii, A.; Malrieu, J.-P. Multi-Partitioning Quasidegenerate Perturbation Theory. A New Approach to Multireference Møller-Plesset Perturbation Theory. *Chem. Phys. Lett.* **1995**, *233*, 597–604.

(28) Finley, J.; Malmqvist, P.-A.; Roos, B. O.; Serrano-Andrés, L. The Multi-State CASPT2 Method. *Chem. Phys. Lett.* **1998**, *288*, 299–306.

(29) Ghigo, G.; Roos, B. O.; Malmqvist, P.-A. A Modified Definition of the Zeroth-Order Hamiltonian in Multiconfigurational Perturbation Theory (CASPT2). *Chem. Phys. Lett.* **2004**, *396*, 142–149.

(30) Hess, B. A.; Marian, C. M.; Wahlgren, U.; Gropen, O. A Mean-Field Spin-Orbit Method Applicable to Correlated Wavefunctions. *Chem. Phys. Lett.* **1996**, *251*, 365–371.

(31) Llusar, R.; Casarrubios, M.; Barandiarán, Z.; Seijo, L. Ab Initio Model Potential Calculations on the Electronic Spectrum of Ni<sup>2+</sup>-Doped MgO Including Correlation, Spin-Orbit and Embedding Effects. *J. Chem. Phys.* **1996**, *105*, 5321–5330.

(32) Malmqvist, P. A.; Roos, B. O.; Schimmelpfennig, B. The RASSI Approach with Spin-Orbit Coupling. *Chem. Phys. Lett.* **2002**, *357*, 230–240.

(33) Paulovic, J.; Nakajima, T.; Hirao, K.; Lindh, R.; Malmqvist, P.-A. Relativistic and Correlated Calculations on the Ground and Excited States of ThO. *J. Chem. Phys.* **2003**, *119*, 798–805.

(34) Roos, B. O.; Lindh, R.; Malmqvist, P. A.; Veryazov, V.; Widmark, P. O. Main Group Atoms and Dimers Studied with a New Relativistic ANO Basis Set. *J. Phys. Chem. A* **2005**, *108*, 2851–2858.

(35) Barandiarán, Z.; Seijo, L. The Ab Initio Model Potential Representation of the Crystalline Environment. Theoretical Study of the Local Distortion on NaCl:Cu<sup>+</sup>. *J. Chem. Phys.* **1988**, *89*, 5739–5746.

(36) Detailed embedding AIMP data libraries in electronic format are available from the authors upon request or directly at the address <http://www.uam.es/quimica/aimp/Data/AIMPLibs.html>. See also ref 18.

(37) Gellé, A.; Lepetit, M.-B. Fast Calculation of the Electrostatic Potential in Ionic Crystals by Direct Summation Method. *J. Chem. Phys.* **2008**, *128*, 244716/1–244716/8.

(38) Ewald, P. P. Die Berechnung Optischer und Elektrostatistischer Gitterpotentiale. *Ann. Phys.* **1921**, *369*, 253–287.

(39) Seijo, L.; Barandiarán, Z. Ab Initio Model Potential Study of Local Distortions Around Cr<sup>+</sup> and Cr<sup>3+</sup>. *J. Chem. Phys.* **1991**, *94*, 8158–8164.

(40) Moore, C. E. Atomic Energy Levels as Derived from the Analysis of Optical Spectra. *Nat. Stand. Ref. Data Ser.* **35**, Vol. III (Reprint of NBS Circ. 467, Vol. III, 1958), 245 pp. (Nat. Bur. Stand., U.S., 1971).

(41) Fleig, T.; Olsen, J.; Marian, C. M. The Generalized Active Space Concept for the Relativistic Treatment of Electron Correlation. I. Kramers-Restricted Two-Component Configuration Interaction. *J. Chem. Phys.* **2001**, *114*, 4775–4790.

(42) Froese-Fischer, C. *The Hartree-Fock Method for Atoms*; John Wiley: New York, 1977.

(43) Dunning, T. H., Jr.; Botch, B. H.; Harrison, J. F. On the Orbital Description of the 4s3d<sup>n+1</sup> States of the Transition Metal Atoms. *J. Chem. Phys.* **1980**, *72*, 3419–3420.

(44) De Jong, M.; Meijerink, M.; Barandiarán, Z.; Seijo, L. *J. Phys. Chem. C*, under review.

(45) Follow the address <http://www.uam.es/departamentos/ciencias/quimica/aimp/Data/MO/> for interactive MO representations. (Accessed April 15, 2014).

(46) Henderson, B.; Imbusch, G. F. *Optical Spectroscopy of Inorganic Solids*; Clarendon Press: Oxford, U.K., 1989.

(47) Pan, F.; Shen, G.; Wang, R.; Wang, X.; Shen, D. Growth, Characterization and Nonlinear Optical Properties of SrB<sub>4</sub>O<sub>7</sub> Crystals. *J. Cryst. Growth* **2002**, *241*, 108–114.

(48) Wolfert, A.; Blasse, G. Luminescence of Bi<sup>3+</sup>-Doped Crystals of Cs<sub>2</sub>NaYBr<sub>6</sub> and Cs<sub>2</sub>NaLaCl<sub>6</sub>. *J. Solid State Chem.* **1985**, *59*, 133–142.

(49) Wolfert, A.; Oomen, E. W. J. L.; Blasse, G. Host Lattice Dependence of the Bi<sup>3+</sup> Luminescence in Orthoborates LnBO<sub>3</sub> (with Ln = Sc, Y, La, Gd, Lu). *J. Solid State Chem.* **1985**, *59*, 280–290.